(article starts on next page)

Fibre orientation distribution function mapping for short fibre polymer composite components from low resolution/large volume X-ray computed tomography

Robert M. Auenhammer [a,b,*], Anuj Prajapati [c], Kaldon Kalasho [d], Lars P. Mikkelsen [b], Philip J. Withers [c], Leif E. Asp [a], Renaud Gutkin [d,a]

[a] Material and Computational Mechanics, Department of Industrial and Materials Science, Chalmers University of Technology, SE-41296 Göteborg, Sweden
[b] Composites Manufacturing and Testing, Department of Wind and Energy Systems, Technical University of Denmark, DK-4000 Roskilde, Denmark
[c] Henry Royce Institute, Dept. of Materials, The University of Manchester, Oxford Road Manchester, M13 9PL, United Kingdom
[d] Safety Centre, Volvo Car Corporation, SE-40531 Göteborg, Sweden

ARTICLE INFO

ABSTRACT

Short glass fibre injection moulded composites, used in interior and exterior automotive parts, are exposed to complex stress states, for example during a crash. As the fibre scale dominates the composite's material properties, numerical models need to account for the local fibre orientation. In recent years, mould flow simulation results have been exploited to predict the fibre orientations for finite element models, albeit with limited accuracy. Alternatively, X-ray computed tomography can be used to directly image and analyse fibre orientations. Traditionally, achieving the necessary resolution to image individual fibres restricts the imaging to small regions of the component. However, this study takes advantage of recent advancements in imaging and image analysis to overcome this limitation. As a result, it introduces, for the first time, a reliable, fast, and automated fibre orientation mapping for a full component based on image analysis at the individual fibre level; even for cases where the pixel size is significantly larger than the fibre diameter. By scanning at lower resolutions, a drastically larger volume of interest can be achieved. The resulting fibre orientation analysis and mapping algorithm, based on X-ray computed tomography, is well matched to the level of information required for automotive crash modelling with a standard element-size of a few millimetres. The entire process, encompassing image acquisition, image analysis and fibre orientation mapping, can be directly integrated into an industrial full component application in a matter of hours.

1. Introduction

Short fibre-reinforced polymers are widely used in the automotive industry as they offer high stiffness and strength at low material and production cost [1]. Injection moulded short fibre composites are used for both interior and exterior parts. As the crash requirements for passenger safety are ever increased [2], short fibre-reinforced polymers with improved crash performance must be realised. By intelligently designing the manufacture of short fibre-reinforced polymers to tailor the fibre directions it is possible to meet the increased crash safety requirements while keeping the weight to a minimum.

Due to the injection moulding process, the fibre orientation distribution is anisotropic [3]. The fibres are predominantly oriented along the flow direction [4], but deviations can easily occur. Since the fibre

orientation is decisive in determining the anisotropic character of fibre-reinforced composites, it is crucial to be able to deal with uncertainties in fibre orientations in the modelling approach for short fibre injection moulded parts [5]. Advani and Tucker [6] originally introduced fibre orientation distribution functions based on flow simulations. With these distribution functions and fibre orientation tensors, the homogenised mechanical properties of a composite can be computed. In automotive industrial development the fibre orientation is commonly not considered and pseudo-isotropic material models based on two-dimensional or three-dimensional random homogenisation used instead. Another option is to use the outcome of mould flow simulations to estimate the fibre orientations and map these onto the integration points of the final finite element mesh [7–10]. This approach eliminates the need for homogenisation of the pseudo-isotropic material model. However,

Table 1
Scanning conditions for the X-ray computed tomography acquisitions on a Thermo Fisher Scientific's Heliscan Mk2.

Voxel size	Sample to source distance	Detector to source distance	Pixel depth	Exposure time	Number projections per revolution	Total number of projections	Accelerating voltage	Tube current
[μm]	[mm]	[mm]		[s]			[kV]	[μA]
20	83	725	16-bit	0.80	1800	4057	80	95
60	97	450	16-bit	0.22	1800	1860	80	95

due to modelling uncertainties [11], e.g., pressure and temperature progression, and changing manufacturing parameters, e.g., humidity, mould wear, mould flow simulation results may be inaccurate.

Due to the described issues associated with mould flow-based modelling, imaging can be used to obtain an improved model once there are parts available. Among numerous imaging techniques, X-ray computed tomography is rapidly becoming the tool of choice for studying composites [12]. Compared to conventional microscopy, the capability of X-ray computed tomography (CT) to non-destructively provide three-dimensional information of the bulk material [13], instead of being limited to surface observations, makes it attractive for studies both on the macro and micro-scale [14]. The resolution of X-ray computed tomography can vary tremendously, ranging from nanometres [15] to a few hundred micrometres [16]. It also provides real-world imaging data on which to build realistic models — incorporating realistic aspects of all phases and imperfections instead of synthetically manufactured data. This enables the prediction of material performance for various material architectures without the need for expensive and time-intensive testing campaigns [17].

There are two fundamentally different methods for X-ray computed tomography-based fibre orientation analysis [18]. One aims to detect each fibre and track it through the three-dimensional image data [19,20] while others use a so-called structure tensor analysis, which estimates the fibre orientations by gradients in the grey-scale values [21–24]. Structure tensor methods come with the advantage that relatively low resolution three-dimensional images still can result in reliable analyses [25]. Recently, Auenhammer et al. [26] reported accurate numerical tensile modulus predictions for a textile composite based on images having voxel-sizes as large as three times the fibre diameter. The change in scanning data size scales with the resolution change cubed. Therefore, even small resolution decreases produce more manageable data-sets or allow for a larger field of view (keeping the same data size).

Finite element simulations of fibrous composites based on X-ray computed tomography or mould flow-based fibre orientation analysis require fibre orientation mapping. Transferring fibre orientation data from image data to numerical models for structural components is in particular challenging due to substantial differences from the μm image scale to the cm component scale. Additionally, finite element models are typically more restricted in terms of manageable numbers of element compared to the number of manageable voxels in imaging. This implies that there is a significantly lower number of elements compared to the number of voxels representing the scanned structure. This limitation is further exacerbated in case the imaged structure is part of a full car model. As a result of the restricted number of manageable elements, finite element models for injection moulded parts in automotive development commonly represent the three-dimensional structure by two-dimensional shell elements. These shell elements typically have a coarse element size ranging from 2 to 4 mm. Considering the scale differences, coarse element size, and two-dimensional representation of the three-dimensional structure, a strategy is essential to effectively transfer all relevant information from the fibre orientation analysis to the final model [27].

The advances in X-ray computed tomography and fibre orientation analysis have opened new possibilities for incorporating fibre orientation data into numerical models at the component level. This study demonstrates the application of an X-ray computed tomography

image-based mapping process to achieve accurate, swift, and automated transfer of low-resolution image data onto a numerical model of a car roof frame part. This process is aimed to be directly applicable to the industrial development process at the component level. While the goal is not to replace mould flow simulation, this method greatly enhances the accuracy of numerical models once physical parts become accessible in the industrial development process.

2. Experimental materials and methods

An injection moulded part reinforced with short glass fibres, as illustrated in Fig. 1, is investigated in this study. The sample is scanned with an X-ray computed tomography lab-based source. The fibre orientations inside the part are analysed for different resolutions and parameters, and then mapped on the target shell mesh.

2.1. Material

The investigated sample is taken from a car roof frame. It is made out of a thermoplastic containing 30% by weight of 20 μm diameter short glass fibres, with a nominal length of 2 mm before processing. Due to the injection moulding process in combination with the low fibre weight fraction it can be assumed that the fibre orientation is inherent to different flow conditions depending mainly on the mould geometry and process condition. Due to the arrangement of the ingate system, whose inlet points fall outside the scanned area, the flow within the scanned part is expected to develop predominately approximately along z-axis in Fig. 1. Consequently, the orientations of the fibres are also anticipated to correspond with this flow direction, albeit with local deviations.

2.2. Scanning

X-ray computed tomography data is acquired on a Thermo Fisher Scientific's Heliscan Mk2, which allows for a helical scanning trajectory to scan tall, high aspect ratio (height to width) samples in a single acquisition. In helical scanning, height limit for a sample is much less compared to the width. For regular micro computed tomography, high aspect ratio samples must be scanned using several single scans which are stitched together. This is cumbersome and can lead to artefacts as well as varying scan quality along the height. With helical scanning image stitching is circumvented. The sample is scanned at two different resolutions, at voxel-sizes of 20 μm and 60 μm. The scanning conditions are listed in Table 1. Two sub-volumes are scanned at a voxel-size of 20 μm. One region is defined around a screwing dome, *Dome Scan*, and the region around supporting ribs is denoted *Rib Scan* (Fig. 1). It is not feasible to scan the entire part at a voxel-size of 20 μm, as the data size would become too large to handle with a size of approximately 100 GB. In Table 2, the data sizes of the five different volume scans are compared. It has to be kept in mind that, a three times increase in voxel-size leads to a 27-times reduction in data size. The scanning time for the full component at a voxel-size of 60 μm has been approximately 1.5 h. The *Rib Scan* and *Dome Scan*, scanned at a voxel-size of 20 μm, have been acquired in approximately 15 and 13 h, respectively.

In the sub-volume *Dome Scan*, three cross-sectional slices, and in the sub-volume *Rib Scan*, six slices are defined for representative comparisons. In Fig. 2, one slice per sub-volume scan is presented as a
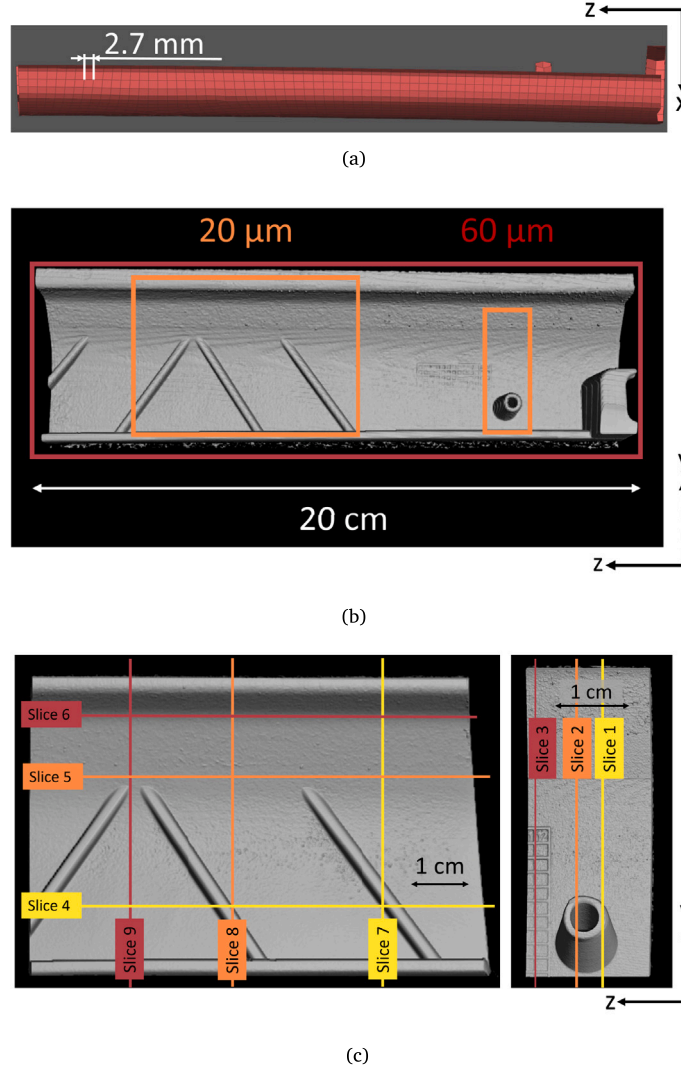
Fig. 1. (a) Target finite element model with mostly quadrilateral two-dimensional shell elements with an average length of approximately 2.7 mm and a thickness of 2.5 mm visualised in the computer aided engineering (CAE) pre-processor ANSA. Spatially one shell element therefore covers approximately 84,000 voxels for a voxel-size of 60 μm. (b) In total three scans are carried out. The full part is scanned with a voxel-size of 60 μm (red box), while the regions around the ribs and the dome are scanned with voxel-sizes of 20 μm (orange boxes). The scans are volume rendered in Thermo Fisher's software package Avizo. (c) Thereby, the two sub-volume scans are available both in voxel-sizes of 20 μm and 60 μm. The left scan is denoted *Rib Scan*, whereas the right scan is denoted *Dome Scan*. For a more detailed analysis in total nine cross-sectional slices through the scans are defined. The cross-sectional slices are analysed further in the Results chapter. (For interpretation of the references to colour in this figure legend, the reader is referred to the web version of this article.)

Table 2
Scanning time, scanned volume and chosen voxel-size. Note that in total five data-sets are available even though only three scans have been acquired. The *Dome Scan* and *Rib Scan* are cropped from the *Full Scan*. Therefore, *Dome Scan* and *Rib Scan* are available at both voxel-sizes which leads to different data sizes.

	Dome Scan	*Rib Scan*	*Full Scan*
Scanning time [h]	13	15	1.5
Scanned volume [mm³]	30.5 × 42 × 16.6	25.4 × 55.4 × 75.8	28.7 × 67.4 × 204
Scanned voxel-size [μm]	20	20	60
Data size [GB]	5.2	34.2	–
Data size [GB]	0.19	1.3	3.5

grey-scale image for both voxel-sizes. The individual fibres cannot be distinguished in either of the scans, but as it has previously been proven, the overall orientations of glass fibres can accurately be captured using voxel-sizes around 20 μm [25,26]. The thin lines at the outer surface of the sample, that are visible in all slices, stem from

the sample's lamination for a nice appearance in the car, and are not considered further in this study.

2.3. Fibre orientation analysis

The fibre orientation analysis is made using the structure tensor code developed by Jeppesen et al. [23,24]. Its robustness, speed and accuracy have been demonstrated in other studies [18,26]. In particular, it allows scans at low resolutions based on a voxel-size of 60 μm. The structure tensor S is calculated as gradient of the greyscale intensity ∇V in a certain area around each voxel (Eq. (1)). For the computation of the gradient and the integration around the regarded point Gaussian kernels are used (Eq. (2)).

$$S = \sum \nabla V (\nabla V)^T. \tag{1}$$

$$S = K_\rho (\nabla V_\sigma (\nabla V_\sigma)^T) \tag{2}$$

The standard deviations of those two Gaussian kernels, σ_{ST} and ρ_{ST}, are the only two parameters required for this method. The noise
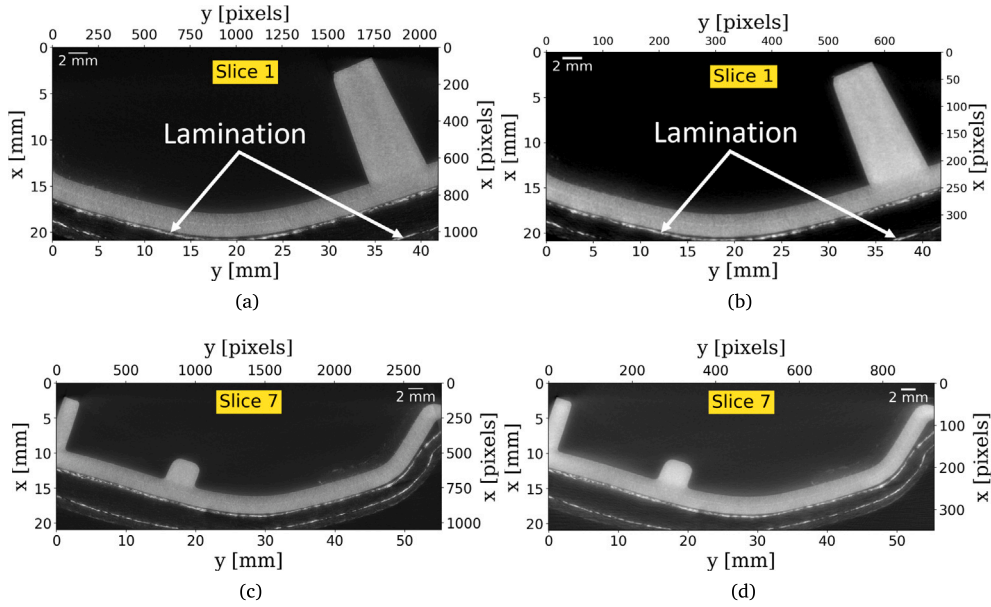
Fig. 2. Representative comparison of the grey-scale Slice 1 in xy-plane in the *Dome Scan* for a voxel-size of 20 μm (a) and 60 μm (b); and Slice 7 in xy-plane in the *Rib Scan* for a voxel-size of 20 μm (c) and 60 μm (d). The thin white lines are part of the lamination of the part for a nicer appearance in the car and are not further considered in this study.

scale parameter σ_{ST} determines the gradient calculation via a first-order derivative of the Gaussian kernel. It should be chosen to be large enough to remove high-frequency image noise, but small enough to account for local fibre orientation gradients. The integration scale parameter ρ_{ST} determines the standard deviation of the Gaussian Kernel for integrating the local orientations in the neighbourhood of the considered integration point. Even though, there are only two parameters, they need to be chosen carefully. Despite the high quality of the image data, a voxel-size of 60 μm is at the limit of what can currently be analysed to obtain a meaningful result. Multiple parameter combinations are tested and compared, for different resolutions and at different locations. In the end it is decided to use $\sigma_{ST} = 0.625$ and $\rho_{ST} = 2.5$ for the scans with a voxel-size of 20 μm, whereas the scan with a voxel-size of 60 μm is analysed with $\sigma_{ST} = 0.5$ and $\rho_{ST} = 1.75$. The influence of these parameter selections is discussed in the Results section.

The eigenvector of the second-order structure tensor S corresponding to the lowest eigenvalue is interpreted as dominant fibre orientation p. This dominant fibre orientation is not to be confused with an orientation vector for a single fibre. Despite the structure tensor S containing information about the anisotropy in fibre orientation within each voxel, we henceforth solely rely on the dominant fibre orientation vector p for all following computations and analyses. It should be noted that this vector still contains the inherent orientation information of multiple fibres. This is a consequence of the characteristics of the structure tensor method, which consistently integrates orientation information from neighbouring voxels. This aspect becomes especially relevant due to the large voxel-size of 60 μm. For a voxel-size this large, roughly three times the diameter of a single fibre, the dominant fibre orientation vector will inevitably represent a homogenised orientation, representing orientation information from multiple fibres.

In this study, the investigation of the image analysis is conducted on the voxel scale. Typically, a distribution of fibre orientations is represented as fibre orientation tensors [6]. However, in this context, only the dominant fibre orientation vector at the voxel scale is available, and it is expressed as a unit vector (Eq. (3)) in Cartesian coordinates [28], where φ represents the in-plane angle between x-axis and the xy-projection of the unit vector, also denoted azimuth, and θ the angle
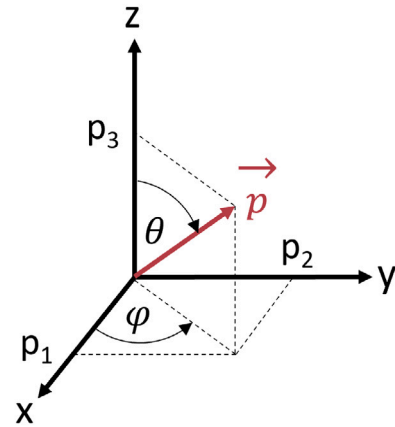

Fig. 3. The fibre orientation can be expressed as a unit vector (Eq. (3)) in Cartesian coordinates, where φ represents the in-plane angle between x-axis and the xy-projection of the unit vector, also denoted azimuth, and θ the angle between the z-axis and the unit vector, also denoted zenith.

between z-axis and the unit vector, also denoted zenith (see Fig. 3).

$$p_i = \begin{Bmatrix} p_1 \\ p_2 \\ p_3 \end{Bmatrix} = \begin{Bmatrix} cos(\varphi)sin(\theta) \\ sin(\varphi)sin(\theta) \\ cos(\theta) \end{Bmatrix} \tag{3}$$

As the fibres are expected to be oriented predominantly along the flow direction, which approximately coincides with the z-direction of the image coordinate system, the absolute value of p_3 is taken (Eq. (4)). This limits the angle range to $[0°, 90°]$ and is thereby a clear indicator for fibre misalignments.

$$\theta = \arccos(|p_3|) \tag{4}$$

The azimuth angle φ is referred to as the in-plane xy angle and is computed according to Eq. (5). Due to the tangent the angle is defined
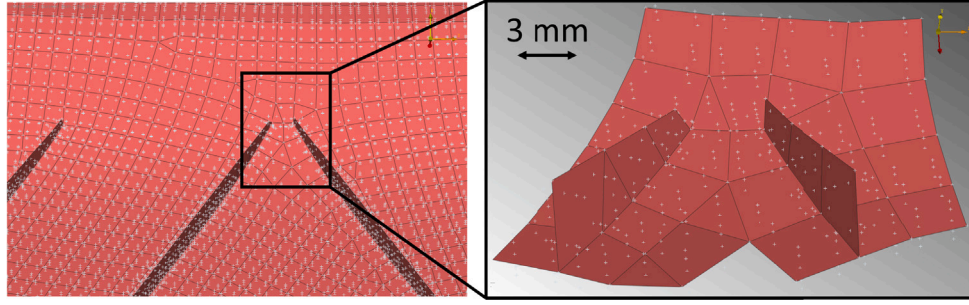
Fig. 4. The grey crosses represent the computed integration point coordinates. Quadrilateral elements have four integration points per element, while triangular elements have only one. In total, there are five integration point layers per element.

within $[-90°, 90°]$.

$$\varphi = \arctan \frac{p_2}{p_1} \qquad (5)$$

The fibre orientation angles are only computed for visualisation, following the procedure suggested by Jeppesen et al. [24]. The final mapping output is computed based on a computation of fibre orientation tensors.

2.4. Mapping

Due to the different scales with small fibres and large element sizes, not all information from the image data can be transferred to the numerical model. Thus, in the mapping process information will be lost. The key is to lose as little relevant information as possible.

In the described mapping process only the *Full Scan* with a voxel-size of 60 μm is used. In the presented simulations, the target mesh primarily consists of quadrilateral two-dimensional shell elements with an average length of approximately 2.7 mm and a thickness of 2.5 mm. Spatially one shell element therefore covers approximately 84,000 voxels for a voxel-size of 60 μm. The quadrilateral shell elements are set up with 2×2 Gaussian integration points at the mid-plane and four additional through-thickness layers resulting in twenty integration points per element. Each integration point thereby spatially represents approximately 4200 voxels. Consequently, an accurate and computationally efficient way must be found to express the orientation of 4,200 voxels in one orientation tensor with six independent components. Additionally, the two-dimensional target shell mesh must be placed exactly on the mid-plane of the three-dimensional image data of the scanned part. There is currently no automated process to carry out this task. Therefore, manual translations and rotations are necessary until a sufficient match is achieved.

For the mapping process, a Python script is developed. It is based on the script described in [29]. Firstly, the translated and rotated target mesh in LS-Dyna format is read-in. Based on the mesh data node/element arrays are created. For each of the elements, an element normal is computed. As the quadrilateral elements are usually warped, this computation is not straightforward. Details on how the element normal is calculated can be found in the LS-Dyna keyword manual [30]. Additionally, for each element, the mid-plane Gaussian integration point coordinates are calculated with the element's shape functions. With the element normals, the integration point coordinates in the four other layers through the thickness are computed. Those integration points are placed at certain distances from the mid-plane, expressed as factors normalised by half of the shell element thickness [±0.906; ±0.538]. In Fig. 4 the integration points for one region of the model are depicted. For the majority of the elements three through-thickness layers with integration points can be seen, the other two layers are hidden behind the shell elements. Finally, the orientation mapping takes place. In a certain domain around each integration point, the estimated material orientation from the image analysis is

homogenised. Computing the average of fibre orientations is a non-trivial operation. Per fibre orientation there are two fibre orientation vectors possible $\boldsymbol{p} = -\boldsymbol{p}$. Therefore, computing the mean of fibre orientation vectors is not constructive; two fibre vectors with the same direction but different sign would cancel each other. The sign issue can be taken care of by computing the square of $\boldsymbol{p}$. The best vector multiplication for this purpose is the dyadic product (Eq. (6)).

$$p_i(\varphi, \theta)p_j(\varphi, \theta) = \begin{bmatrix} p_1 p_1 & p_1 p_2 & p_1 p_3 \\ p_2 p_1 & p_2 p_2 & p_2 p_3 \\ p_3 p_1 & p_3 p_2 & p_3 p_3 \end{bmatrix} \qquad (6)$$

In combination with a fibre orientation probability distribution function $\Psi(\boldsymbol{p})$ a so-called second-order orientation tensor (Eq. (7)), first proposed by Advani and Tucker [6], can be computed.

$$A_{ij} = \oint p_i p_j \, \Psi(\boldsymbol{p}) \, d\boldsymbol{p}, \qquad (7)$$

With a finite amount of fibre orientation vectors, one per voxel in this study, the orientation tensor can be calculated as the mean sum the dyadic product (Eq. (8)). In the context of this study, it is important to note that N represents the number of voxels. Each voxel is associated with a dominant fibre orientation vector $\boldsymbol{p}$, where this vector represents the orientation of multiple fibres. Consequently, Eq. (8) can be understood as an averaging for all fibre orientations within a certain domain.

$$A_{ij} = \langle p_i p_j \rangle = \frac{1}{N} \sum_{k=1}^{N} (p_i p_j)_k \qquad (8)$$

In order to investigate the influence of the homogenisation domain the fibre orientation tensors are computed for five different areas, whereas one of them only considers one voxel. The other four cases average the fibre orientations of 27, 125, 729 and 3375 voxels, respectively, around each integration point. For each integration point the orientation tensors are stored in a binary file that can be directly read-in in an LS-Dyna simulation.

3. Results

Different scans are studied here. For the sub-volumes *Dome Scan* and *Rib Scan*, the fibre orientation distributions are analysed. Additionally, for the sub-volumes *Dome Scan* and *Rib Scan* several cross-sectional slices are defined to compare the local accuracy within a cross-sectional slice for the different resolutions. For the *Rib Scan*, the influence of the structure tensor parameters is examined. For the *Full Scan*, the fibre orientations and the mapping process are analysed. The fibre orientation distributions are compared using histograms showing the in-plane xy angle φ and the z-off axis angle θ for the two voxel-sizes 20 μm and 60 μm.
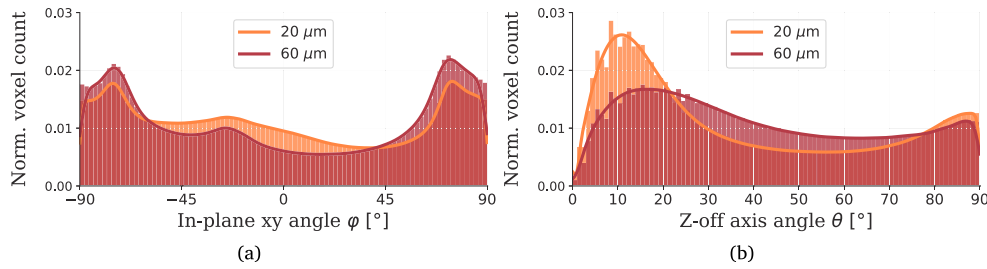
Fig. 5. Histograms of the in-plane xy (azimuthal) angle φ (a) and z-off axis (zenith) angle θ (b) for the *Dome Scan* for the two voxel-sizes 20 μm and 60 μm. The solid lines represent Gaussian Kernel density estimations. The voxel counts are normalised for better comparison.
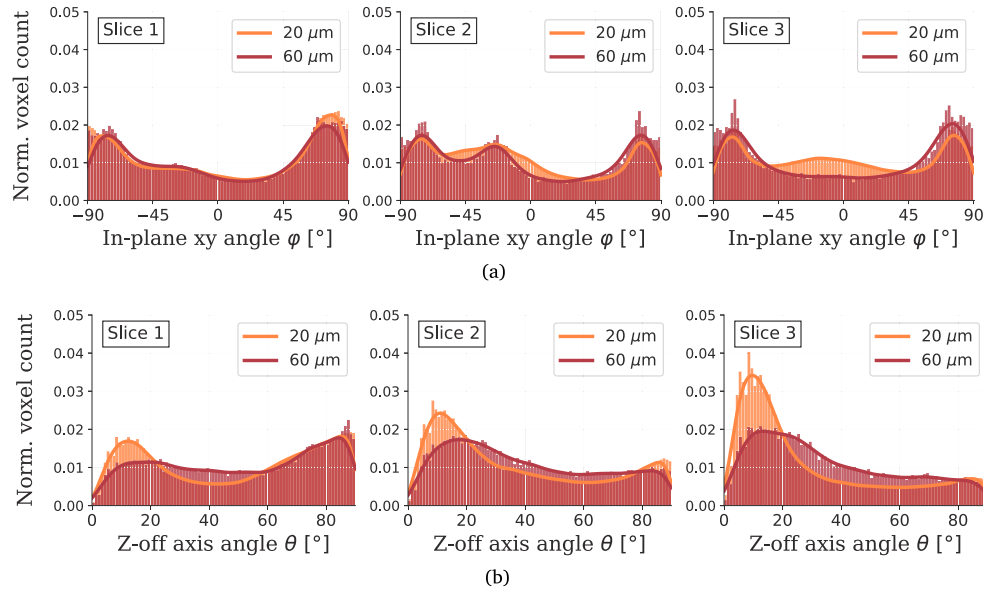
Fig. 6. Histograms of the in-plane xy (azimuthal) angle φ (a) and z-off (zenith) axis angle θ (b) for the defined three slices in the *Dome Scan* and the two voxel-sizes 20 μm and 60 μm. The solid lines represent Gaussian Kernel density estimations. The voxel counts are normalised for better comparison.

3.1. Dome Scan

For the full sub-volume of the *Dome Scan* the in-plane xy angle φ and z-off axis angle θ histograms are depicted in Fig. 5 for both voxel-sizes 20 and 60 μm. Overall the angles for the two resolutions match well. Given that a substantial portion of voxels within this scan depict the dome area where fibres are predominantly oriented circumferentially, the z-off axis angle θ histogram does not exhibit a pronounced orientation along the *z*-axis. For the in-plane xy (azimuthal) angle φ, the two significant peaks at approximately ±80° are overestimated in the low-resolution scan. In contrast, for the z-off axis (zenith) angle θ, the peaks at approximately 10° and 90° are underestimated.

However, a favourable match in the histograms for the sub-volume does not provide an absolute confirmation that the distributions of fibre orientations, primarily influenced by factors such as mould geometry and process conditions under different flow conditions, align perfectly. It is conceivable that a histogram may occasionally exhibit a satisfactory match purely by chance, despite underlying fibre orientation distribution disparities. Hence, the comparison of the fibre orientations for both voxel-sizes is extended to local cross-sectional slices with histograms and plots exhibiting the fibre orientation per voxel. This not only provides additional validation for the accuracy of the fibre orientation analysis but also facilitates the examination of factors contributing to both underestimation and overestimation through these local cross-sectional slices. The in-plane xy angle φ is captured well in Slice 1 and 2, which include the dome itself (Fig. 6a). In Slice 3, which lies outside the dome, the overestimation of the peaks at ±80° for the voxel-size of 60 μm is more distinct. For the z-off axis angle θ,

a similar picture is obtained. The histograms for Slice 1 and 2 show a good match, while the peak at approximately 10° is underestimated using a voxel-size of 60 μm (Fig. 6b). These results can be explored using the plots presented in Fig. 7. One notable feature that becomes apparent is the presence of a clearly distinguishable off-axis mid-layer. This mid-layer, commonly referred to as the core layer in literature, is formed as a result of the injection moulding process [31]. In the case of short fibre injection moulded parts, three distinct regimes are typically observed: the aforementioned core layer, the shell layer predominantly oriented along the flow direction, and a thin skin layer formed due to thermal shock resulting from colder mould walls [32]. Among these three layers, the shell layer is the thickest, while the skin layer is the thinnest. In the studied sample the skin layer is not very pronounced, and can be hardly resolved in the low-resolution scans. Inside the dome, the orientations match very well. As they represent a significant part of the scan, the angles match also well in the histogram. However, in the bulk part of the material outside the core layer, there are some off-axis fibres identified. These small domains are amplified in the scan with 60 μm. This leads to a shift from close to zero angles to larger angles and an underestimation of the peaks at approximately 10° in the histograms.

In general, it can be observed that for the *Dome Scan* the orientations for both voxel-sizes match well. However, the obstacle for the mould flow created by the dome leads to a less uniform fibre orientation distribution. This non-uniform fibre orientation distribution is more challenging for the low-resolution scan to capture.
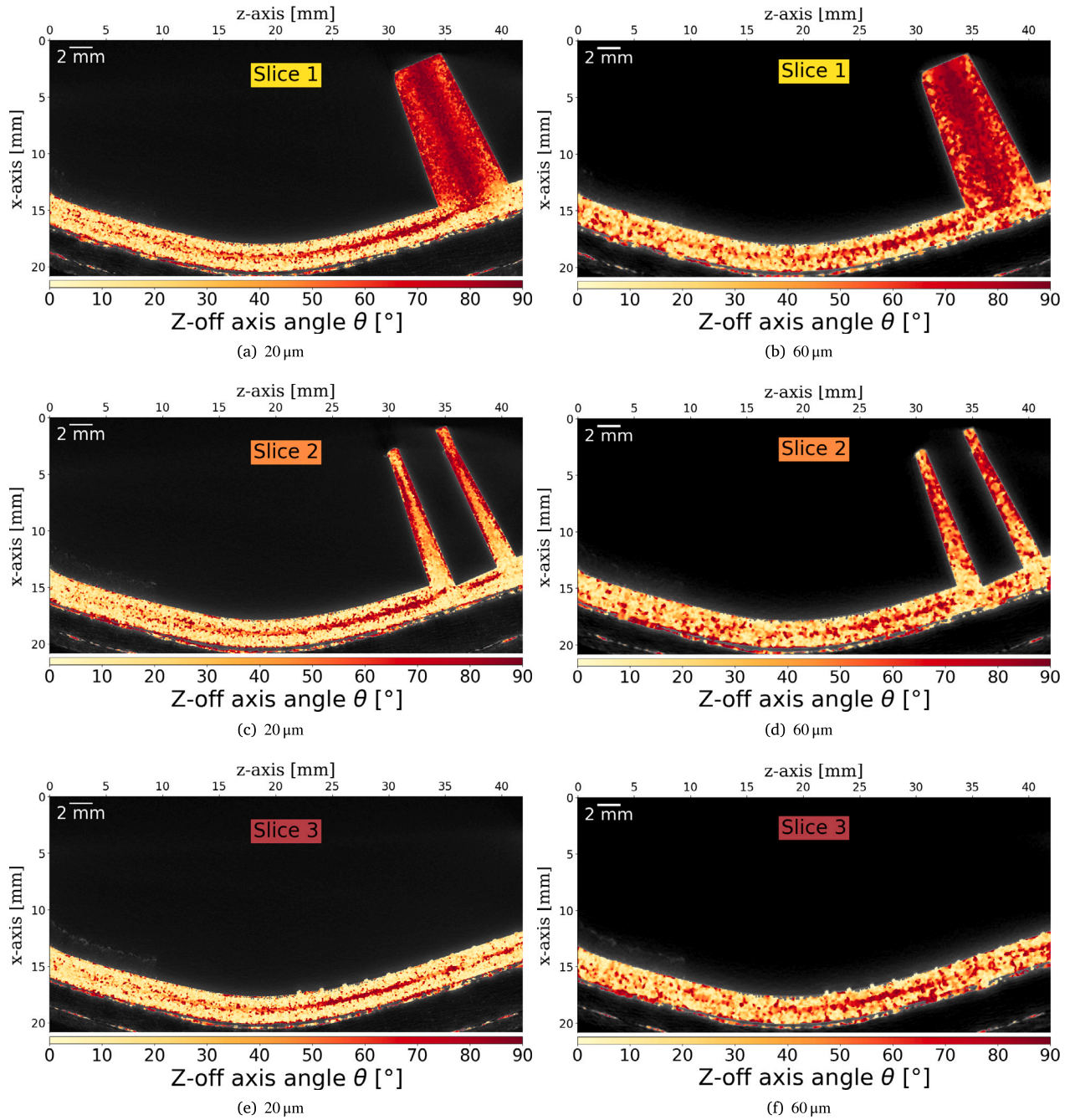
Fig. 7. Comparison of the z-off axis (zenith) angle θ colour-mapped onto the original grey-scale images for Slice 1–3 in the *Dome Scan* for the two voxel-sizes 20 μm and 60 μm.
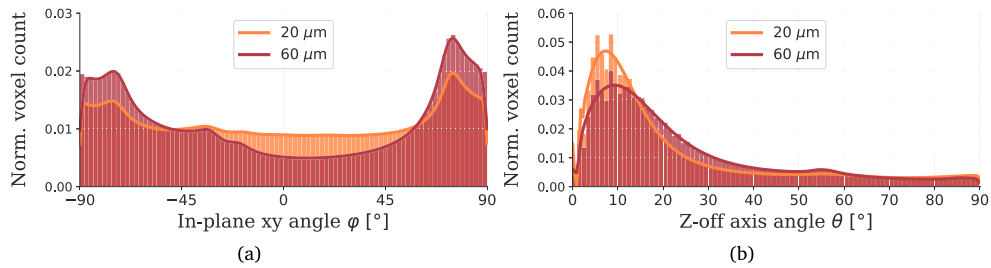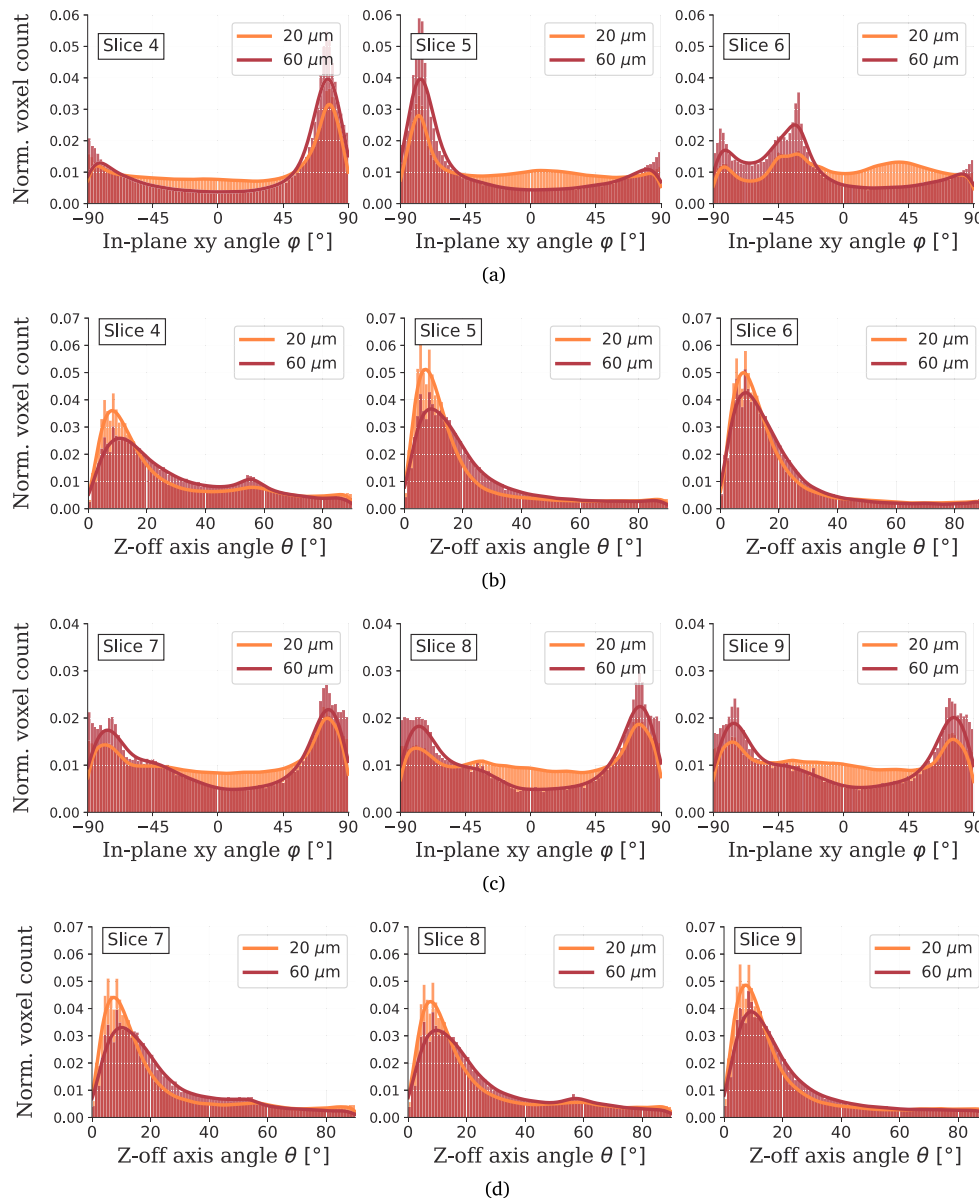

Fig. 8. Histograms of the in-plane xy (azimuthal) angle φ (a) and z-off axis (zenith) angle θ (b) for the *Rib Scan* for the two voxel-sizes 20 μm and 60 μm. The solid lines represent Gaussian Kernel density estimations. The voxel counts are normalised for better comparison.

Fig. 9. Comparison of the in-plane xy (azimuthal) angle φ (a) and (c) and z-off axis (zenith) angle θ (b) and (d) for Slices 4–9 in the *Rib Scan* and the two voxel-sizes 20 μm and 60 μm. The solid lines represent Gaussian Kernel density estimations. The voxel counts are normalised for better comparison.

3.2. Rib Scan

Overall, the orientation distributions in the *Rib Scans* match well for the two different voxel-sizes. The match between low and high-resolution scans is even improved compared to the *Dome Scan*. The low-resolution scan overestimates the peaks of the in-plane xy angle φ at approximately ±80° (Fig. 8a). For the z-off axis angle θ, the peak at approximately 10° is only slightly underestimated (Fig. 8b).

Also, for the more local analysis of the single cross-sectional Slices 4–9 the outcome is similar. The low-resolution scan overestimates the peaks in the in-plane xy angle φ histograms (Fig. 9a,c), while the peak in the z-off axis angle θ is slightly underestimated (Fig. 9 b,d).

The z-off axis angle θ colour-mapped onto the original grey-scale images shows a very good match for the two different voxel-sizes (Fig. 10). Here, the fibre orientations are more uniform compared to those in the *Dome Scan*. Therefore, the match between the two different voxel-sizes is also better. Furthermore, Fig. 10 illustrates a discernible spatial tilt of the component from right to left. Consequently, the predominant flow direction, which primarily follows the component, deviates somewhat

from alignment with the image *z*-axis. This discrepancy serves as the primary explanation for the subtle displacement of the peak in the z-off axis angle θ histogram, which is shifted to around 5–10°. Moreover, even in cases involving highly aligned fibres, such as in [33], there is an notable shift of the peak in the z-off axis angle θ histogram by 1–2°.

An additional effect associated with low-resolution scans becomes apparent in Fig. 9, 10. To induce the appearance of minor misalignment spots or even noise in the low-resolution scan, it is essential that these imperfections are depicted by a pixel area nine times larger in the low-resolution scan compared to the high-resolution scan. Consequently, smaller areas of misalignment become magnified in the low-resolution scans. This effect also clarifies the reason behind the overestimation of peaks in the histograms for the in-plane xy angle φ, while concurrently underestimating the peak in the z-off axis angle θ histogram.

Given the overall stochastic nature of the in-plane xy angle φ distribution, the two minor peaks, signifying fibre misalignment, are intensified. Conversely, for the *z*-axis off angle θ, the distribution is relatively consistent along the *z*-axis. As a result, deviations from the central axis are accentuated, leading to an underestimation of the
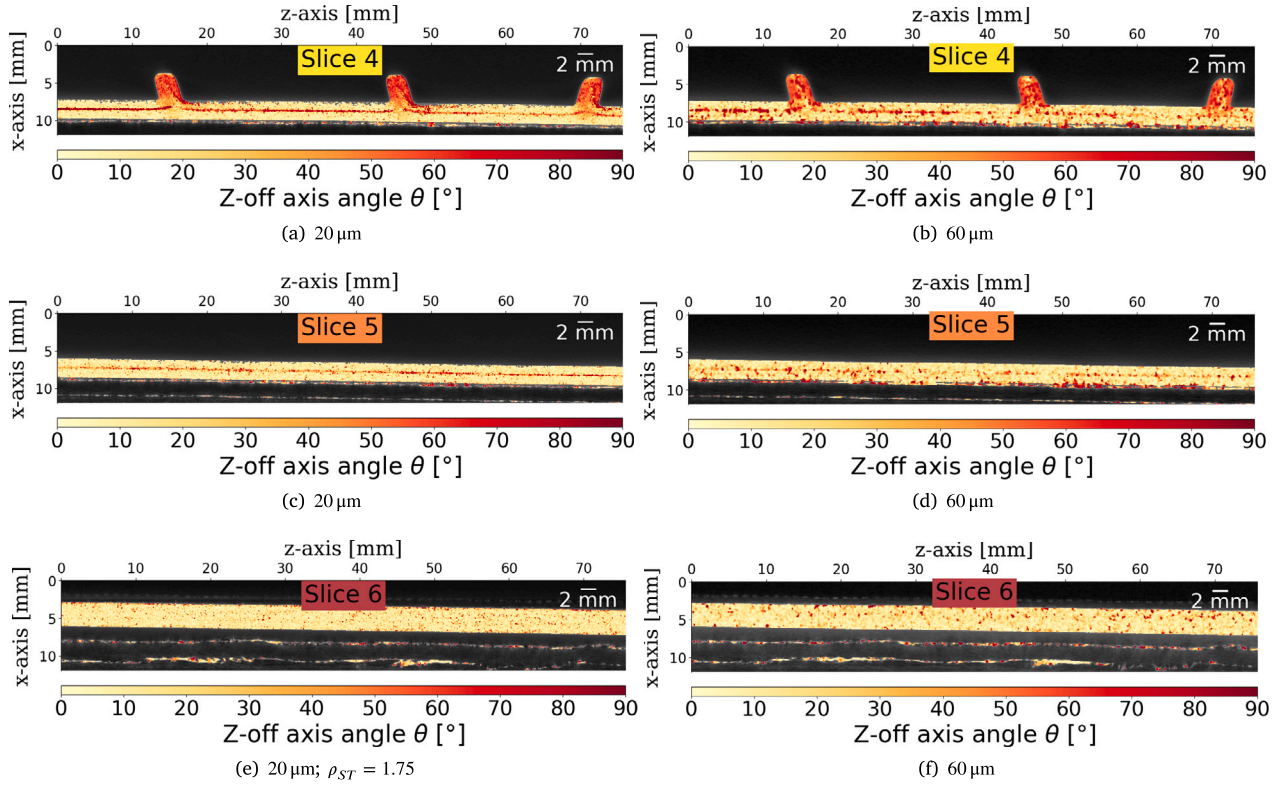
Fig. 10. Comparison of the z-off axis (zenith) angle θ mapped onto the original grey-scale images for Slice 4–6 in the *Rib Scan* for the two voxel-sizes 20 μm and 60 μm.

peak at approximately 5–10°. The adjustment of the structure tensor parameters can mitigate this effect, which is discussed in greater detail in the subsequent section.

3.3. Structure tensor parameters

The influence of the structure tensor parameters σ_{ST} and ρ_{ST} is visualised for Slice 4 in the *Rib Scan* with a voxel-size of 60 μm in Figs. 11 and 12. The low resolution introduces noise. With the noise scale parameter σ_{ST} this effect can be minimised. However, both a too small (Fig. 11a,b) and too high σ_{ST} (Fig. 11e,f) values fail to remove this noise.

Similarly the effect of the integration scale parameter ρ_{ST} is analysed. If the integration domain, represented by the integration scale parameter ρ_{ST}, is too small, the orientations become completely random, and only local noise is recorded (Fig. 12a,b). When a sufficiently large integration scale parameter is chosen, the effect of noise is reduced. However, if ρ_{ST} is chosen too large, any off-axis orientations will be suppressed (Fig. 12i,j).

Based on the outcome of this parameter study, $\sigma_{ST} = 0.5$ and $\rho_{ST} = 1.75$ are chosen. This choice offers a good compromise between noise reduction and capture of local fibre misalignments. For the case illustrated in Fig. 12, a larger ρ_{ST} provides a better match with the high-resolution scan results. However, as presented in the *Dome Scan* analysis there are issues with the given choice of the structure tensor parameter pair capturing the local fibre orientations in the more non-uniformly distributed areas.

3.4. Mapping

In Fig. 13 the three a_{ii} components of the second-order orientation tensor (Eq. (8)) are compared for the entire image data-set (voxel-size 60 μm) and the voxels that spatially encompass an integration point. Notably, no homogenisation has been applied in this instance.

Consequently, only the orientation information from the voxel containing the target integration point is considered for the comparison. It is worth noting that there are approximately 210 million voxels, each carrying a dominant fibre orientation vector, available for the mapping process. In contrast, there are only approximately 43 thousand target integration points. Despite the substantial difference of a factor of approximately 4800 between the number of voxels and the target integration points, it is worth noting a meaningful correspondence between the fibre orientation distribution in the original image data and that within the voxels containing an integration point. While this alignment could be attributed to pure randomness, it is more plausible that it stems from the presence of larger regions within the scanned specimen showcasing a consistent fibre orientation distribution. Additionally, the placement of five integration points across the wall thickness contributes to capturing diverse orientations, including those of the core layer. Moreover, it is crucial to acknowledge that even initial factors, such as the substantial voxel size and inherent aspects of the structure tensor analysis, introduce a form of homogenisation.

The influence of the homogenisation area in the mapping process is studied in Fig. 14. Here, the three a_{ii} components of the second-order orientation tensor of mapped orientations are compared for different homogenisation areas. For this purpose for each integration point the mean of the fibre orientations of 27, 125, 729 and 3375 voxels, respectively, is computed. Naturally, during the mapping and homogenisation information is lost. On the basis of up to several thousand dominant fibre orientation vectors only one second-order orientation tensor per integration point can be mapped. From Fig. 14 it becomes evident that the size of the homogenisation area has a substantial influence on the orientation tensors. With larger homogenisation areas the fibre orientation along z-axis, represented by component a_{33}, becomes less prominent. In general, selecting a larger homogenisation area incorporates more information. However, opting for an excessively large homogenisation area runs the risk of suppressing local deviations.
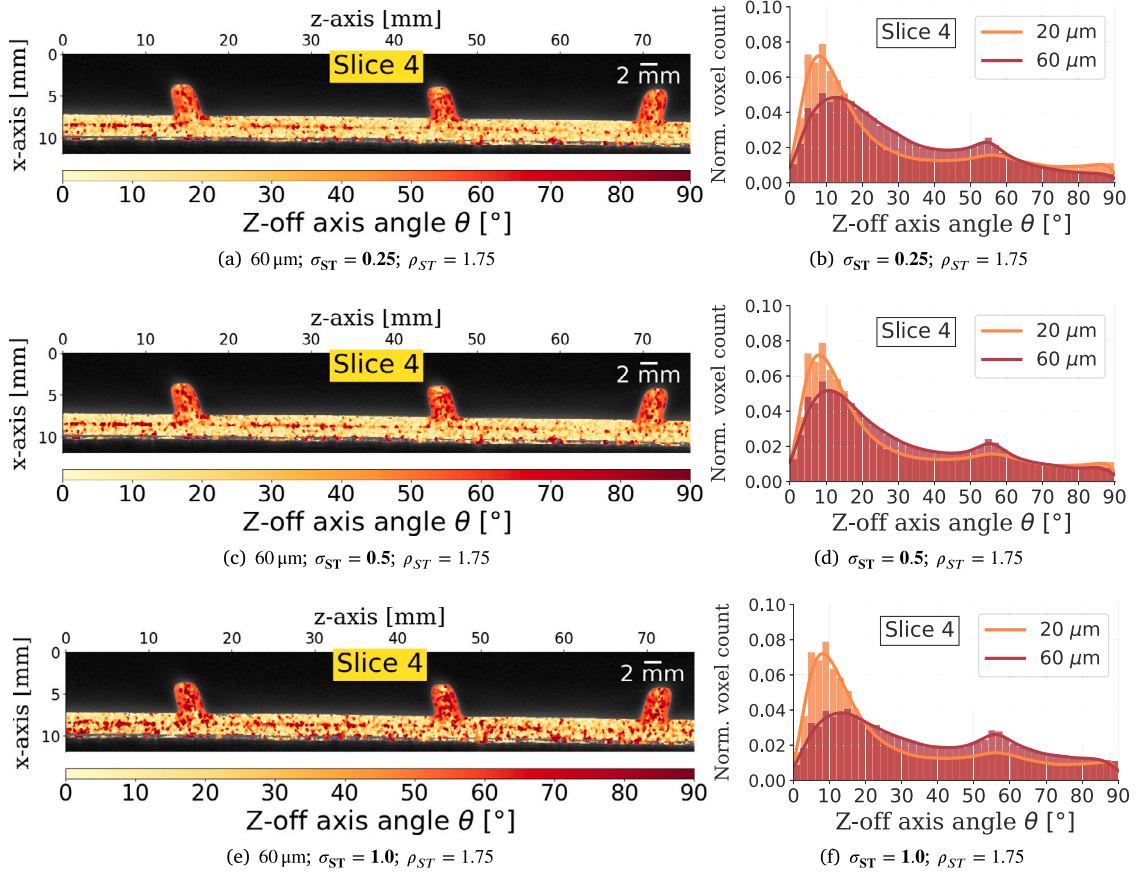
Fig. 11. Comparison of the z-off axis (zenith) angle θ colour-mapped onto the original grey-scale images for a voxel-size of $60\,\mu m$ (left) and histograms (right) for Slice 4 in the *Rib Scan* for different values of the structure tensor parameter σ_{ST}. The structure tensor parameters σ_{ST} and ρ_{ST} for the histogram of the voxel-size of $20\,\mu m$ are unchanged at $\sigma_{ST} = 0.625$ and $\rho_{ST} = 2.5$. The solid lines in the histograms are Gaussian Kernel density estimations.

The final selection of the homogenisation area size depends on the particular modelling goal. In applications such as predicting compressive strength [33], where even a small number of misaligned fibres can lead to failure, choosing a homogenisation area that is too large might yield a mean value incapable of accurately predicting failure. Conversely, in predicting tensile modulus, wherein all fibres contribute significantly, it becomes essential to utilise larger homogenisation areas.

In Fig. 15 the outcome of the fibre orientation mapping is visualised in the computer aided engineering (CAE) pre-processor ANSA. For the depicted mapping result no homogenisation has been applied. For the majority of the elements only three through-thickness layers are shown. The remaining two lie hidden behind the shell elements. Overall, the fibres are oriented along the *z*-axis in areas where the mould flow has developed nearly undisturbed. The small clip housing in the lower left corner (Fig. 1a), the dome and the ribs act as obstacles, that disturb the mould flow and by that the fibre orientation. Additionally, it can be noted that there is a significant difference between the individual layers. These observation can be also seen in the slices through the sub-volume scans (Figs. 7 and 10).

4. Discussion

Typically, micro X-ray computed tomography scans of fibrous composites are conducted to analyse the micro-structure at the individual fibre level. This level of analysis provides valuable insights into the composite's characteristics. However, a high resolution (a fine pixel size) is necessary for such scans. Although there are no technical limitations preventing the acquisition of high-resolution scans, the field of view is significantly restricted (a few millimetres in such a case).

In the context of this study, the objective has been to perform a complete component scan and analysis, rather than focusing solely on the micro-structure at the fibre level. Therefore, this study aims to bridge the gap between two significantly different length scales. On one side, there are the glass fibres that, according to state-of-the-art approaches, require voxel-sizes smaller than half the fibre diameter for proper imaging resolution. On the other side, there is the structural part, 20 cm in length, with a given coarse mesh with an average element length of 2.7 mm.

In case a state-of-the-art approach with a resolution of approximately $10\,\mu m$ in voxel-size as for example in [17] had been chosen, the resulting three-dimensional image data-set would have consisted of a staggering 45 billion voxels. This data-set would have then needed to be mapped onto the 43,180 target integration points, resulting in approximately 1,000,000 voxels per integration point. However, it has been shown that we can exploit the structure tensor method and apply much lower resolutions. By employing lower resolutions, the number of required voxels is reduced to approximately 210 million, resulting in a factor of 4800 instead of 1,000,000 voxels per integration point. This significant reduction in voxel count greatly improves both data
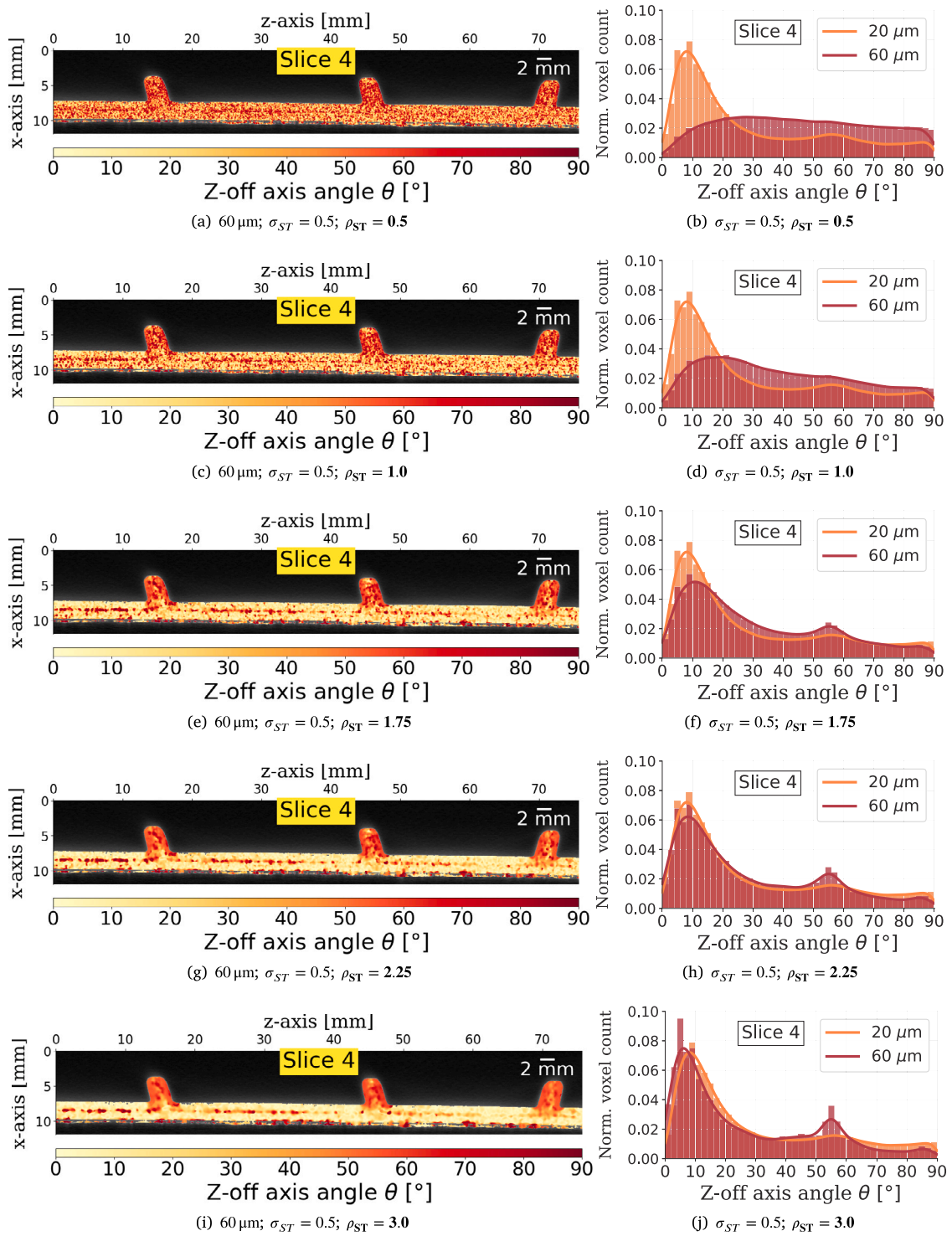
Fig. 12. Comparison of the z-off axis (zenith) angle θ colour-mapped onto the original grey-scale images for a voxel-size of $60\,\mu m$ (left) and histograms (right) for Slice 4 in the *Rib Scan* for different values of the structure tensor parameter ρ_{ST}. The structure tensor parameters σ_{ST} and ρ_{ST} for the histogram of the voxel-size of $20\,\mu m$ are unchanged at $\sigma_{ST} = 0.625$ and $\rho_{ST} = 2.5$. The solid lines in the histograms represent Gaussian Kernel density estimations.

acquisition and computational costs, making studies of this nature feasible.

Although the fibre orientation distributions obtained from the scans with resolutions of $20\,\mu m$ and $60\,\mu m$ show good agreement, it is important to note that this study is pushing the resolution limits for accurately processing the orientation of glass fibres using existing fibre orientation analysis codes. The lower resolution chosen in this study is a compromise. While it allows for feasibility in terms of processing

and computational requirements, it also results in a loss of accuracy compared to high-resolution scans.

However, in any case, either for low or high-resolution scans, information will be lost during the mapping process as the fidelity level of the finite element model is significantly lower than the fidelity of the image data. In other words; detailed information from high-resolution scans cannot be represented in the final model in any case. Therefore, to achieve a successful transfer of information from the image data-set
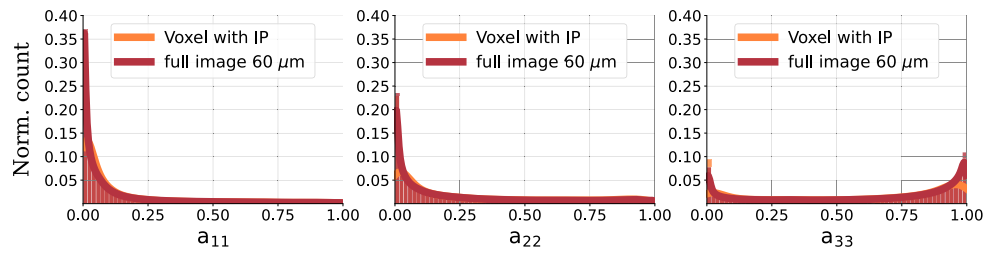
Fig. 13. Histograms of the three a_{ii} components of the second-order orientation tensor (Eq. (8)) computed for the full three-dimensional image data-set (207,660,459 voxels with a voxel-size of $60\,\mu m$) and for 43,180 voxels which spatially contain an integration point (IP). Note, each second-order orientation tensor (Eq. (8)) is computed based on one dominant fibre orientation vector $\boldsymbol{p}$. Both counts in the histogram are normalised for better comparison. The solid lines represent Gaussian Kernel density estimations.
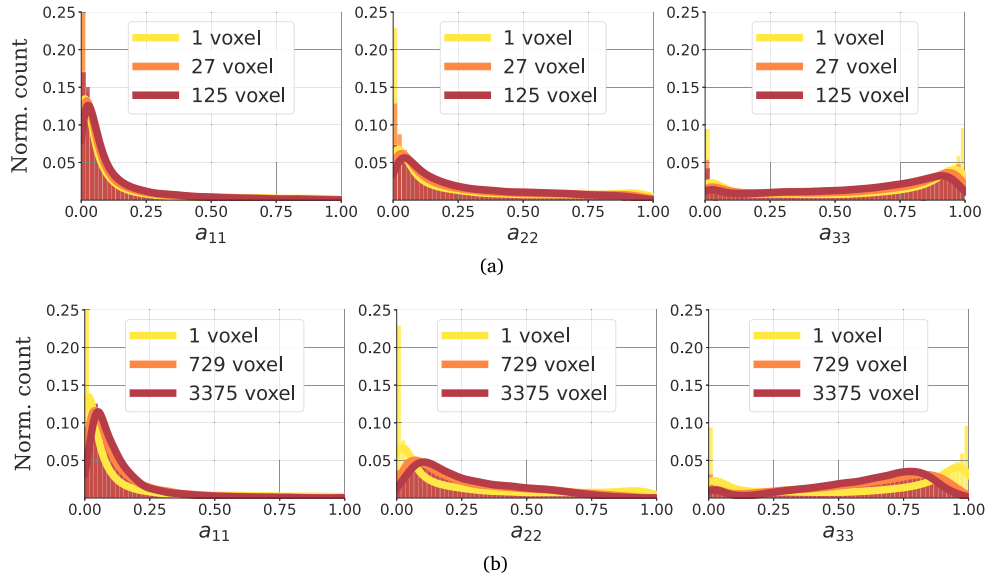
Fig. 14. Histograms of the three a_{ii} components of the mapped second-order orientation tensor (according to Eq. (8)) for five different areas. The fibre orientation tensors are mapped onto 43,180 target integration points. The results for '1 voxel' (yellow curves) are computed based on one dominant fibre orientation vector $\boldsymbol{p}$ of the voxel, the target integration point lies in. (a) Three different areas where two (orange and red curve) homogenise fibre orientations of 27 and 125 voxels, respectively, around the target integration points. (b) Three different areas where two (orange and red curve) homogenise fibre orientations of 729 and 3375 voxels, respectively, around the target integration points. The solid lines represent Gaussian Kernel density estimations. (For interpretation of the references to colour in this figure legend, the reader is referred to the web version of this article.)

to the final model, a holistic approach is crucial. This entails ensuring alignment and coherence among various factors, including imaging techniques, structure tensor parameters (σ_{ST} and ρ_{ST}), and mapping homogenisation parameters.

A final conclusion or recommendation cannot be stated here, as the homogenisation area also needs to be chosen with respect to the material model and the overall modelling goal. Those latter two aspects are not part of this study and hence it remains for further research to investigate those aspects.

With low-resolution scans, noise is introduced in the three-dimensional image data. For the structure tensor method, it becomes challenging to differentiate between actual noise and diverging local fibre orientations. With an appropriate choice of the structure tensor parameters, this effect can be reduced, but never eliminated. Additionally, no special low-resolution image reconstruction algorithm has been used. It remains for further work to investigate the influence of the reconstruction algorithm.

Overall, the presented choice of both the structure tensor parameters and the mapping homogenisation, are considered to be the most suitable compromise for this case. However, it has been shown that in areas with higher fibre orientation gradients, the structure tensor parameters σ_{ST} and ρ_{ST} should be smaller, while in regions, where the flow can develop undisturbed, the parameters can be selected to be larger. Locally different parameters depending on the fibre gradient can be implemented in future work.

In the presented workflow, three instances of fibre orientation consolidations occur. The first occurs during the scanning process due to its inherent low resolution, resulting in a grey-scale intensity at the detector that already represents smoothed fibre orientations. The second homogenisation takes place during the structure tensor analysis, where also neighbouring voxels influence the dominant fibre orientation in the regarded voxel. Lastly, the fibre orientations are averaged during the mapping phase, where fibre orientation tensors are utilised.

The mapping process has also been compared with the commercial software Digimat [34], but the process in Digimat remains opaque. On the other hand, the developed method provides an elegant and efficient solution for complete control over the mapping process. This is advantageous because it ensures alignment between the structure tensor parameters and the mapping parameters. If the structure tensor analysis covers a larger integration area, the mapping homogenisation domain should be smaller, as both steps involve homogenisation. Initially, orientations within the three-dimensional image data are homogenised, subsequently, those homogenised orientations are further homogenised for each integration point. If the homogenisation regions are too large, the mean orientations of the entire part may become smeared. However, if the regions are too small, noise from the image data may be introduced into the final model.

Injection moulding is a complex process and depends on manifold parameters. However, mould flow simulations are widely used and can deliver accurate process predictions. Nonetheless, due to the
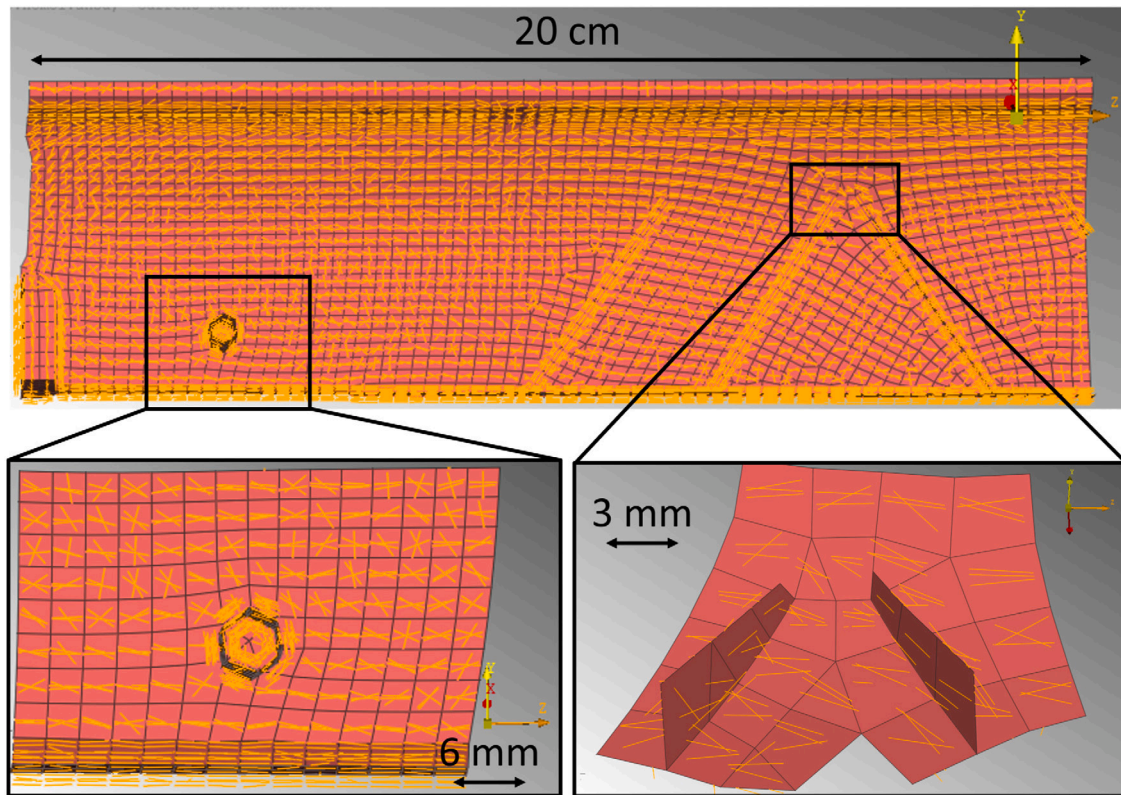
Fig. 15. Mapped fibre orientations onto the two-dimensional shell mesh with five integration point layers over the thickness visualised in the computer aided engineering (CAE) pre-processor ANSA. No fibre orientation homogenisation has been used in this case, e.g., only the fibre orientation of the voxel the target integration point lies in has been mapped. The orange lines represent the mean fibre orientation per integration point layer. Note, this is only for visualisation. In fact, the mapping algorithm assigns an individual fibre orientation to each integration point. In the case of quadrilateral elements, twenty individual orientations are assigned (five through-thickness layers with four integration points each). (For interpretation of the references to colour in this figure legend, the reader is referred to the web version of this article.)

complexity of the mould flow process the simulated fibre orientations risk to be inaccurate. Here, the enormous possibilities of modern X-ray computed tomography in combination with accurate image analysis and fibre orientation mapping are demonstrated. Nevertheless, imaging cannot replace mould flow simulations, as there must be a physical part available to scan. In the long-term both methods will complement each other. The accuracy of mould flow simulations can be improved by large field-of-view image analyses. At the same time, the definition of the structure tensor and mapping homogenisation parameters can be improved based on mould flow fibre orientation results. However, also this aspect remains for further research. In the end it will lead to virtual parts with higher maturity in the initial development phases, and improved crash models once physical prototypes are available.

While a primary objective of this study is to establish an initial framework for seamlessly integrating X-ray computed tomography-based fibre orientation mapping into an automotive crash model, the knowledge gained and methodologies developed possess the capacity to be effortlessly applied to a diverse range of other low-resolution image-based numerical models. Nonetheless, a cautious approach is imperative during the final integration process. Despite the demonstrated accuracy and robustness, the incorporated mapped fibre orientations contain inherent uncertainties. Those uncertainties should be duly acknowledged in the final model. Therefore, it is advisable to formulate a material model that accounts for those uncertainties.

5. Conclusions

This study exploits the current progress in imaging and image analysis to introduce for the first time an accurate, swift, and automated fibre orientation mapping based on low-resolution X-ray computed tomography data for a full component. An injection moulded glass

fibre-reinforced thermoplastic containing $20 \mu m$ diameter fibres is studied by way of an example. Despite the low resolution of $60 \mu m$ in voxel-size the applied robust structure tensor image analysis method accurately captures the fibre orientation distribution. While this resolution fails to capture the orientation of every fibre, the approach is commensurate with the resolution that numerical models of composites in industrial applications can efficiently handle from a computation viewpoint. The developed mapping algorithm successfully transfers the high-fidelity image information comprising approximately 210 million voxels onto a numerical model with approximately 43 thousand integration points. The entire image analysis and mapping process for the studied sample with a length of $20 \, cm$ takes approximately 10 min on a standard personal computer.

CRediT authorship contribution statement

Robert M. Auenhammer: Writing – review & editing, Writing – original draft, Visualization, Validation, Software, Methodology, Investigation, Formal analysis. **Anuj Prajapati:** Writing – review & editing, Writing – original draft, Visualization, Validation, Methodology, Investigation. **Kaldon Kalasho:** Validation, Software, Investigation. **Lars P. Mikkelsen:** Writing – review & editing, Validation, Supervision, Funding acquisition. **Philip J. Withers:** Writing – review & editing, Validation, Supervision, Funding acquisition. **Leif E. Asp:** Writing – review & editing, Validation, Supervision, Funding acquisition. **Renaud Gutkin:** Writing – review & editing, Validation, Supervision, Funding acquisition.

Declaration of competing interest

The authors declare that they have no known competing financial interests or personal relationships that could have appeared to influence the work reported in this paper.

Data availability

The authors do not have permission to share data.

Appendix A. Supplementary data

Supplementary material related to this article can be found online at https://doi.org/10.1016/j.compositesb.2024.111313.

References

[1] Castagnet S, Nadot-Martin C, Fouchier N, Conrado E, Bernasconi A. Fatigue life assessment in notched injection-molded specimens of a short-glass fiber reinforced Polyamide 6 with different injection gate locations. Int J Fatigue 2021;143:105968. http://dx.doi.org/10.1016/j.ijfatigue.2020.105968.

[2] Regulation (EU) 2019/2144 of the European Parliament and of the Council. Off J Eur Union 2019.

[3] Wei H, Wu CT, Hu W, Su T-h, Oura H, Nishi M, et al. LS-DYNA machine learning – based multiscale method for nonlinear modeling of short fiber – reinforced composites. J Eng Mech 2023;149:04023003. http://dx.doi.org/10.1061/JENMDT.EMENG-6945.

[4] Li Z, Lu J, Qiu R, Liu Z, Zhu P. Multiscale modeling based failure criterion of injection molded SFRP composites considering skin-core-skin layered microstructure and variable parameters. Compos Struct 2022;286:115277. http://dx.doi.org/10.1016/j.compstruct.2022.115277.

[5] Guo FL, Hu JM, Guan T, Fu YT, Huang CY, Li YQ, et al. Modeling and characterizations of mechanical behaviors of short carbon fiber and short glass fiber reinforced polyetherimide composites. Compos Sci Technol 2022;229:109685. http://dx.doi.org/10.1016/j.compscitech.2022.109685.

[6] Advani SG, Tucker CL. The use of tensors to describe and predict fiber orientation in short fiber composites. J Rheol 1987;31:751–84. http://dx.doi.org/10.1122/1.549945.

[7] Foss PH, Tseng H-C, Snawerdt J, Chang Y-J, Yang W-H, Hsu C-H. Prediction of fiber orientation distribution in injection molded parts using Moldex3D simulation. Polym Polym Compos 2014;35:671–80. http://dx.doi.org/10.1002/pc.22710.

[8] Mosey S, Korkees F, Rees A, Llewelyn G. Investigation into fibre orientation and weldline reduction of injection moulded short glass-fibre/polyamide 6-6 automotive components. J Thermoplast Compos Mater 2020;33:1603–28. http://dx.doi.org/10.1177/0892705719833098.

[9] Quagliato L, Kim Y, Fonseca JH, Han D, Yun S, Lee H, et al. The influence of fiber orientation and geometry-induced strain concentration on the fatigue life of short carbon fibers reinforced polyamide-6. Mater Des 2020;190:108569. http://dx.doi.org/10.1016/j.matdes.2020.108569.

[10] Żurawik R, Volke J, Zarges JC, Heim HP. Comparison of real and simulated fiber orientations in injection molded short glass fiber reinforced polyamide by X-ray microtomography. Polymers 2022;14:29. http://dx.doi.org/10.3390/polym14010029.

[11] Saad S, Sinha A, Cruz C, Régnier G, Ammar A. Towards an accurate pressure estimation in injection molding simulation using surrogate modeling. Int J Mater Form 2022;15:72. http://dx.doi.org/10.1007/s12289-022-01717-0.

[12] Naresh K, Khan KA, Umer R, Cantwell WJ. The use of X-ray computed tomography for design and process modeling of aerospace composites: A review. Mater Des 2020;190:108553. http://dx.doi.org/10.1016/j.matdes.2020.108553.

[13] Zwanenburg EA, Williams MA, Warnett JM. Review of high-speed imaging with lab-based X-ray computed tomography. Meas Sci Technol 2022;33:012003. http://dx.doi.org/10.1088/1361-6501/ac354a.

[14] Maire E, Withers PJ. Quantitative X-ray tomography. Int Mater Rev 2014;59:1–43. http://dx.doi.org/10.1179/1743280413Y.0000000023.

[15] Takahashi K, Shoya R, Matsuo T, Sato W, Nakamura T, Takeuchi A, et al. X-ray nanoimaging of a transversely embedded carbon fiber in epoxy matrix under static and cyclic loads. Sci Rep 2022;12:8843. http://dx.doi.org/10.1038/s41598-022-12724-1.

[16] Garcea S, Wang Y, Withers P. X-ray computed tomography of polymer composites. Compos Sci Technol 2018;156:305–19. http://dx.doi.org/10.1016/j.compscitech.2017.10.023.

[17] Auenhammer RM, Mikkelsen LP, Asp LE, Blinzler BJ. Automated X-ray computer tomography segmentation method for finite element analysis of non-crimp fabric reinforced composites. Compos Struct 2021;256:113136. http://dx.doi.org/10.1016/j.compstruct.2020.113136.

[18] Salling FB, Jeppesen N, Sonne MR, Hattel JH, Mikkelsen LP. Individual fibre inclination segmentation from X-ray computed tomography using principal component analysis. J Compos Mater 2021;56:83–98. http://dx.doi.org/10.1177/00219983211052741.

[19] Emerson MJ, Jespersen KM, Dahl AB, Conradsen K, Mikkelsen LP. Individual fibre segmentation from 3D X-ray computed tomography for characterising the fibre orientation in unidirectional composite materials. Composites A 2017;97:83–92. http://dx.doi.org/10.1016/j.compositesa.2016.12.028.

[20] Emerson MJ, Dahl VA, Conradsen K, Mikkelsen LP, Dahl AB. Statistical validation of individual fibre segmentation from tomograms and microscopy. Compos Sci Technol 2018;160:208–15. http://dx.doi.org/10.1016/j.compscitech.2018.03.027.

[21] Krause M, Hausherr JM, Burgeth B, Herrmann C, Krenkel W. Determination of the fibre orientation in composites using the structure tensor and local X-ray transform. J Mater Sci 2010;45:888–96. http://dx.doi.org/10.1007/s10853-009-4016-4.

[22] Straumit I, Lomov SV, Wevers M. Quantification of the internal structure and automatic generation of voxel models of textile composites from X-ray computed tomography data. Composites A 2015;69:150–8. http://dx.doi.org/10.1016/j.compositesa.2014.11.016.

[23] Jeppesen N, Dahl VA, Christensen AN, Dahl AB, Mikkelsen LP. Characterization of the fiber orientations in non-crimp glass fiber reinforced composites using structure tensor. IOP Conf Ser Mater Sci Eng 2020;942:012037. http://dx.doi.org/10.1088/1757-899x/942/1/012037.

[24] Jeppesen N, Mikkelsen LP, Dahl AB, Christensen AN, Dahl VA. Quantifying effects of manufacturing methods on fiber orientation in unidirectional composites using structure tensor analysis. Composites A 2021;149:106541. http://dx.doi.org/10.1016/j.compositesa.2021.106541.

[25] Karamov R, Martulli LM, Kerschbaum M, Sergeichev I, Swolfs Y, Lomov SV. Micro-CT based structure tensor analysis of fibre orientation in random fibre composites versus high-fidelity fibre identification methods. Compos Struct 2020;235:111818. http://dx.doi.org/10.1016/j.compstruct.2019.111818.

[26] Auenhammer RM, Jeppesen N, Mikkelsen LP, Dahl VA, Blinzler BJ, Asp LE. Robust numerical analysis of fibrous composites from X-ray computed tomography image data enabling low resolutions. Compos Sci Technol 2022;224:109458. http://dx.doi.org/10.1016/j.compscitech.2022.109458.

[27] Isaincu A, Dan M, Ungureanu V, Marsavina L. Numerical investigation on the influence of fiber orientation mapping procedure to the mechanical response of short-fiber reinforced composites using Moldflow, Digimat and Ansys software. Mater Today Proc 2021;45:4304–9. http://dx.doi.org/10.1016/j.matpr.2020.12.792.

[28] Bay RS, Tucker CL. Fiber orientation in simple injection moldings. Part I: Theory and numerical methods. Polym Compos 1992;13:317–31. http://dx.doi.org/10.1002/pc.750130409.

[29] Auenhammer RM, Jeppesen N, Mikkelsen LP, Dahl VA, Asp LE. X-ray computed tomography data structure tensor orientation mapping for finite element models — STXAE. Softw Impacts 2022;11:100216. http://dx.doi.org/10.1016/j.simpa.2021.100216.

[30] LS-DYNA Manual R13.0 Vol I. 2023, https://www.dynasupport.com/manuals/ls-dyna-manuals/ls-dyna_manual_volume_i_r13.pdf/view. (Accessed 28 March 2023).

[31] Bernasconi A, Cosmi F, Dreossi D. Local anisotropy analysis of injection moulded fibre reinforced polymer composites. Compos Sci Technol 2008;68(12):2574–81. http://dx.doi.org/10.1016/j.compscitech.2008.05.022.

[32] Rolland H, Saintier N, Robert G. Damage mechanisms in short glass fibre reinforced thermoplastic during in situ microtomography tensile tests. Composites B 2016;90:365–77. http://dx.doi.org/10.1016/j.compositesb.2015.12.021.

[33] Ferguson OV, Skovsgaard SP, Jensen HM, Mikkelsen LP. Compressive strength prediction of carbon fiber-reinforced pultruded profiles including realistic volumetric fiber orientations. Eur J Mech A Solids 2023;105011. http://dx.doi.org/10.1016/j.euromechsol.2023.105011.

[34] Digimat product documentation: 2023 release. 2023, https://simcompanion.hexagon.com/customers/s/article/Digimat-Product-Documentation-2023-Release. (Accessed 02 April 2023).